Flow structure and modeling issues in the closure region of attached cavitation

Shridhar Gopalan and Joseph Katz
Department of Mechanical Engineering, The Johns Hopkins University, Baltimore, Maryland 21218

(Received 20 May 1999; accepted 13 December 1999)

Particle image velocimetry (PIV) and high-speed photography are used to measure the flow structure at the closure region and downstream of sheet cavitation. The experiments are performed in a water tunnel of cross section 6.35×5.08 cm^2 whose test area contains transparent nozzles with a prescribed pressure distribution. This study presents data on instantaneous and averaged velocity, vorticity and turbulence when the ambient pressure is reduced slightly below the cavitation inception level. The results demonstrate that the collapse of the vapor cavities in the closure region is the primary mechanism of vorticity production. When the cavity is thin there is no reverse flow downstream and below the cavitation, i.e., a reentrant flow does not occur. Instead, the cavities collapse as the vapor condenses, creating in the process hairpin-like vortices with microscopic bubbles in their cores. These hairpin vortices, some of which have sizes as much as three times the height of the stable cavity, dominate the flow downstream of the cavitating region. The averaged velocity distributions show that the unsteady collapse of the cavities in the closure region involves substantial increase in turbulence, momentum, and displacement thickness. Two series of tests performed at the same velocity and pressure, i.e., at the same hydrodynamic conditions, but at different water temperatures, 35 °C and 45 °C, show the effect of small changes in the cavitation index (σ=4.69 vs. σ=4.41). This small decrease causes only a slight increase in the size of the cavity, but has a significant impact on the turbulence level and momentum deficit in the boundary layer downstream. Ensemble averaging of the measured instantaneous velocity distributions is used for estimating the liquid void fraction, average velocities, Reynolds stresses, turbulent kinetic energy and pressure distributions. The results are used to examine the mass and momentum balance downstream of the cavitating region. It is shown that in dealing with the ensemble-averaged flow in the closure region of attached cavitation, one should account for the sharp (but still finite) gradients in the liquid void fraction. The 2-D continuity equation can only be satisfied when the gradients in void fraction are included in the analysis. Using the momentum equation it is possible to estimate the magnitude of the ''interaction term,'' i.e., the impact of the vapor phase on the liquid momentum. It is demonstrated that, at least for the present test conditions, the interaction term can be estimated as the local pressure multiplied by the gradient in void fraction. [S1070-6631(00)00804-7]

I. INTRODUCTION

Sheet cavitation appears on lifting surfaces as the pressure on parts of the body, typically near the leading edge, is reduced below the vapor pressure. At early phases, when the cavitation index is just below the inception level, the cavity is typically thin and has a glossy leading edge with either a blunt front or a series of sharp thin ''fingers.'' Their occurrence depends on the surface roughness (a discussion follows). The liquid–vapor interface becomes wavy, unstable and eventually breaks up at the trailing edge (closure region) of the vapor sheet. The flow downstream of the cavity is dominated by bubble clusters and contains, even in mild cases, large-scale eddies (for example, Ref. 1) that are more powerful (i.e., strength and size are larger) than any boundary layer structure that exists prior to the cavitation. At the present time we have no substantiated quantitative or qualitative explanation for these phenomena and their relationships to the body geometry, boundary layer structure, etc.

The development of attached cavitation from nuclei in flows with laminar separation was demonstrated first by Arakeri and Acosta[2] and later confirmed by Gates and Acosta[3] and Katz.[4] They showed that ''band type cavitation'' occurred as free stream bubbles were entrained into the separated region through the reattachment zone, where they were pushed upstream by the reverse flow. Within the relative quiescent flow of the separated region the bubbles grew slowly. These observations provided for the first time a clue on the process of sheet formation. However, they were also puzzling, since sheet cavitation occurs on surfaces without laminar separation. Thus, the basic mechanism of sheet formation in attached flows remains unanswered.

If the cavitation nucleus is a free stream bubble, it is typically separated from the solid boundary by some liquid. The attachment of this bubble to the surface and the mechanism that prevents the bubbles from being swept away, as demonstrated by Li and Ceccio,[5] are unresolved issues. The process must involve favorable conditions that may include the local pressure distribution, boundary layer thickness, super-saturation (supply of gas) and local surface imperfec-

tion. The latter creates localized flow separation with the associated quiescent region, where bubbles may grow without being swept away. Note also that the presence of a cavitation bubble near the surface changes the local flow structure, and may cause local boundary layer separation. It is well established that the size and shape of surface roughness affect the conditions for inception.[6] The origin of cavitation can also be a surface nucleus, such as air pockets in cracks on the model.[7] Acosta and Hamaguchi[8] demonstrated the effect of surface nuclei. They coated a model with a thin film of silicon oil (which dissolves large amounts of air), and demonstrated that, as long as the film was new, it had significant impact on the inception indices. Peterson[9] showed similar effects by degassing the surface of a body.

Predictions of the length of the cavity have been mostly based on potential flow analysis and empirical data (Refs. 10–14 and a summary by Wu[15]). Recently, Laberteaux and Ceccio[16] compared measured results to theoretical predictions and showed major discrepancies. Of the past efforts to model the flow one should mention the singularity methods of Furness and Hutton[17] and the bubble two-phase flow model developed by Kubota *et al.*[18] The latter followed earlier experiments (Ref. 1) that had demonstrated that the flow rolled up to large vortex structures as the cavity surface became unstable. Their model predicted the unsteady shedding process in the closure region of the cavity. However, the origin of the vorticity causing the rollup was still in the boundary layer upstream of the cavitation and the rollup occurred as the shear layer (interface) became unstable. As will be shown in this paper, although some vorticity is generated in the boundary layer upstream, the dominant origin of the vorticity downstream of the cavitation is the collapse of cavities in the closure region. It is also worthwhile to mention that not all sheet cavities necessarily shed cloud cavitation. Some cavities are ''closed,'' especially those forming on three-dimensional test objects.

As the pressure is reduced the cavitating region grows and becomes increasingly unstable. Portions of the cavity are being shed in larger sections and at lower frequencies to form large bubbly clouds. This shedding process involves substantial changes to the length of the attached sheet. The development, motion and collapse of the cloud is the most destructive form of cavitation. We have very little data or even qualitative understanding of the breakdown of the cavitation and the bubble size distribution within the cloud. Surface pressure fluctuations measured under the cloud are extremely high.[19,20] The flow mechanism causing these high-pressure fluctuations is also unclear, and the current models are based on the assumption that they are caused by shock waves that develop within the bubble cloud (for example, Refs. 21–25).

The shedding process of large sections of the cavity has puzzled researchers for quite a while. If potential flow analysis is used, there must be an unsteady reverse flow in the closure area and below the cavity. Thus, it has been argued that the shedding is caused by a ''reentrant jet,'' a reverse flow that forms below the cavity and ''pinches'' it intermittently (Refs. 1, 17, 18, 20, and 26–32 and many others). Velocity measurements performed by Kawanami *et al.*[20] provided evidence of reverse flow with magnitude of the same order as the free stream velocity. They also showed that small fences installed on the wall, close to the point where the sheet cavitation ended, prevented the shedding of cloud cavitation. The noise levels and drag force also decreased. Callenaere *et al.*[32] demonstrated the upstream motion of the contact point of the cavity with the wall prior to cloud shedding. However, they mention that when the cavity is thin there can be a situation where adverse pressure gradients are too weak for a reentrant jet. This situation is consistent with the present observations that at early stages of cavitation there is no reverse flow below or downstream of the attached cavitation.

The present paper describes part of our on-going effort to resolve the flow structure around and downstream of sheet cavitation. We use PIV to map the flow (instantaneous and mean), vorticity and turbulence as the cavitation index is reduced below the inception level. We provide evidence that the collapse of the cavities is a primary source of vorticity and that small change in the size of the cavity cause substantial increase in the turbulence level and momentum thickness in the boundary layer downstream. We then address modeling issues of the ensemble-averaged flow.

II. EXPERIMENTAL APPARATUS AND INSTRUMENTATION

A. Test facility

To provide detailed answers on the flow structure, it is convenient to perform the experiments in an apparatus that allows careful observations on the flow structure and bubble distribution. Some of the measurements must be performed at a very high magnification under controlled conditions that include boundary layer thickness and characteristics, local pressure gradients, surface roughness and properties, population of nuclei, etc. However, the facility must also allow operations at relevant Reynolds numbers ($>10^6$). These considerations have led to the design of the present experimental apparatus. A schematic description of the test facility is provided in Fig. 1 and the test section is described in more detail in Fig. 2. The pumps are located 5 m below the test section, reducing the likelihood of pump cavitation, and the 1000 ℓ tank is used for separating undesired free stream bubbles. The settling chamber contains screens and honeycombs to reduce the turbulence level (along with the 9:1 contraction) and the vertical tank above is used for controlling the pressure in the facility. The 6.35×5.08 cm^2 test section has a minimum length of 41 cm and maximum entrance velocity of 13 m/sec. Thus, it enables generation of boundary layers with Reynolds numbers (based on axial distance) well into the 10^6 range. Windows on all sides and a transparent contoured nozzle (which is actually part of the bottom window) enable unobstructed observations from all directions.

The contoured surfaces in the test section were designed using a commercial CFD code (*Fluent Inc.*). We chose pressure distributions that resemble a typical suction side of lifting surfaces at incidence. This typical pattern includes a region with low speed (stagnation), sharp decrease in pressure

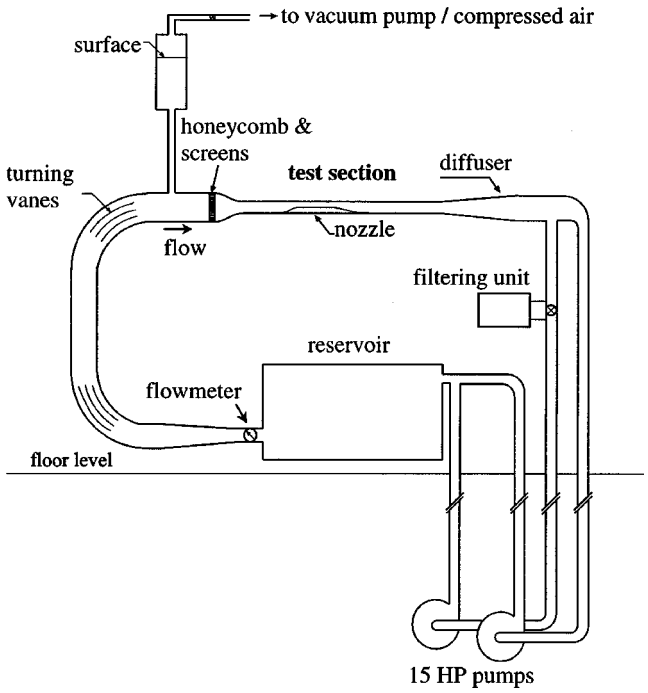

FIG. 1. Schematic description of the experimental facility.

to a minimum, recovery to a pressure lower than the ambient pressure, a region of fairly constant low pressure and further increase to the ambient conditions. The computational grid was made sufficiently fine that further refinement did not affect the results and we used renormalization group (RNG) for turbulence modeling. We assumed a free stream turbulence level of 1% (in reality it is significantly lower—about 0.1%) and a uniform inflow to the test section. A turbulent boundary layer was used since the beginning of the nozzle was located 10 in. from the origin of the test section. Slits on the top and bottom walls of the tunnel, located upstream of the nozzle, were used for boundary layer suction. This was used for determining the effect of the boundary layer on the cavitation (qualitative observations only). In reality, the boundary layer turned out to be laminar. If we had to repeat the design, we would use a laminar boundary layer. Systematic evaluation of a series of designs eventually led to the geometries and pressure distributions shown in Fig. 3 (they are all fifth-order polynomials). They have different pressure gradients and minimum levels, but similar recovery at the trailing edge. Four nozzles identified as shapes 13, 14, 19 and 22 were manufactured using computer numerical control (CNC) at an accuracy of 0.03 mm. As noted before, the

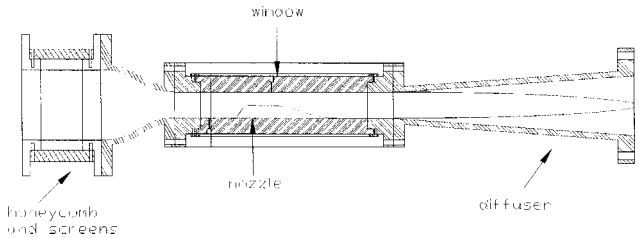

FIG. 2. Details of the test section.

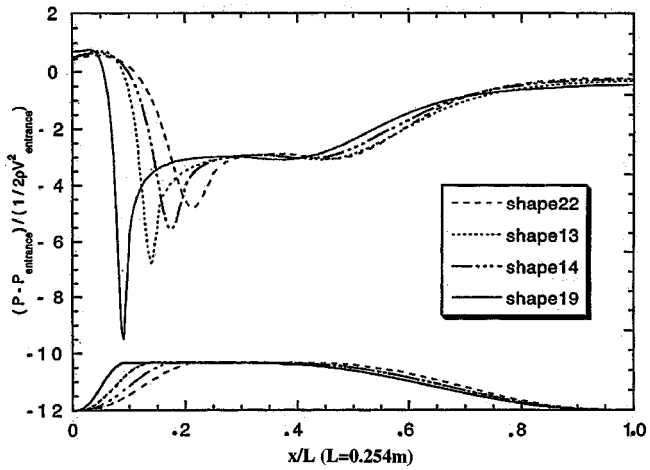

FIG. 3. Geometry of the nozzle surface and the corresponding pressure distributions.

nozzle and the bottom window were machined as one unit to allow unobstructed visual access and to prevent inaccuracies associated with matching them. For one of these cases (shape 13) we compared the computed velocity to measured data and that will be discussed shortly.

B. Measurement techniques

Planar velocity measurements are performed using PIV. The data acquisition and analysis procedures have been developed in our laboratory for several years.[33–41] In the present experiments the light source is a dual head, 300 mJ/pulse, Nd:YAG laser whose beam is expanded to a 1-mm wide sheet. Images are recorded using a 2048×2048 pixels,[2] 4 frames/sec, digital camera manufactured by Silicon Mountain Design. This camera has a custom, hardware-based image shifter that allows us to record two images on the same frame with a prescribed, fixed displacement (image shift) between them).[42] This feature solves the directional ambiguity problem. We use in-house-developed, correlation-based software for computing the velocity distributions from the images. The vorticity is determined using a second-order finite difference scheme. Calibrations and uncertainties of our procedures are discussed in detail in Refs. 33, 39, and 43. Extended discussion on uncertainty in PIV measurements can be found also in Refs. 44 and 45. The uncertainty can be kept at about 1% provided there are a sufficient number of particles per interrogation window (~4–5 according to our analysis) and the displacement between exposures exceeds 20 pixels. In the PIV analysis of the present flow the size of an interrogation window is 1.35 mm and the distance between vectors is 0.68 mm, i.e., 50% overlap between windows.

As discussed by Sridhar and Katz,[39,40] by using fluorescent particles as velocity tracers we can easily distinguish between bubbles and particles within the illuminated plane. Bubbles reflect light, and as a result, maintain the original laser color (green—532 nm), whereas the particles fluoresce at 560–570 nm. During liquid velocity measurements we use a filter that removes the green light, which eliminates most of the bubble traces. When the bubble motion is measured, we

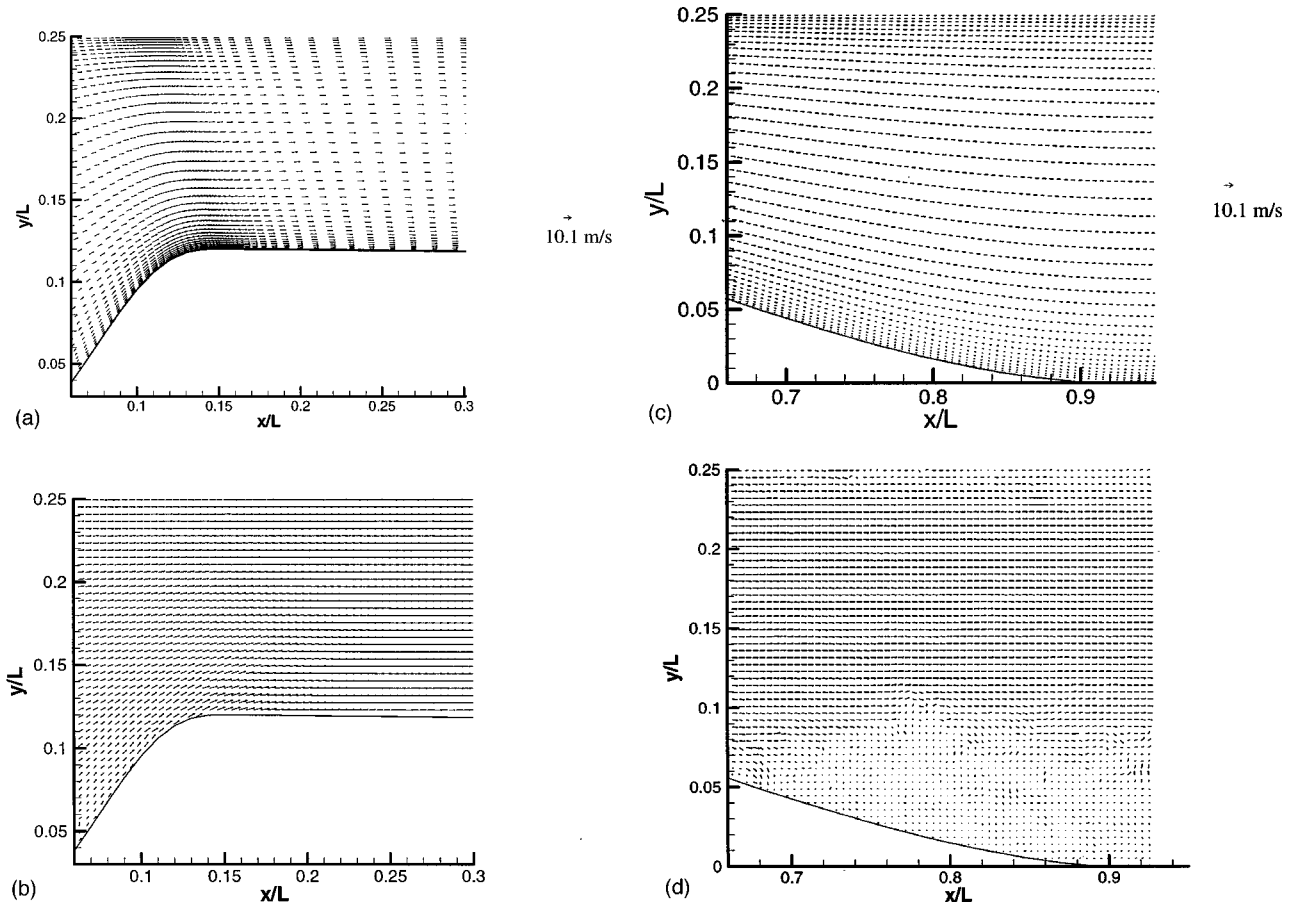

FIG. 4. (a) Computed velocity field using Fluent. (b) Instantaneous measured velocity using PIV. (c) Computed velocity field downstream. (d) Instantaneous measured velocity field downstream.

can use a filter that transmits only the laser wavelength (reflection from the microscopic particles is weak).

III. CAVITATION INCEPTION INDICES AND GENERAL FEATURES

Although detailed validation of the computed pressure distributions is beyond the present scope, it is still useful to compare the measured minimum pressure to the computed data in order to verify the pressure field. The computed velocity distribution and sample instantaneous PIV data, both for shape 13, are presented in Fig. 4. Near the minimum pressure point the ratio of the (maximum) instantaneous velocity to the inlet velocity is 2.4, whereas this ratio for the computed velocity averaged over the area covered by the interrogation window is 2.23. Even this 7% difference is caused in part by the thicker (turbulent) computational boundary layer, whereas the experimental boundary layer is laminar. Consistent with the numerical results, boundary layer separation does not occur in the high adverse pressure gradients downstream of the minimum pressure point. Further downstream, at $x/L>0.58$ [Fig. 4(d), data shown from $x/L=0.66$], the experimental results show the effect of boundary layer transition in a region with adverse pressure gradients, with the typical rollup of large-scale eddies close to the inflection point in the boundary layer mean velocity profile. The mean velocity in this region is still positive, namely there is no boundary layer separation. Note that transition occurs also on the upper wall at almost the same axial location, but with a thinner layer. The numerical results, being steady and with an initially turbulent boundary layer, do not show these trends [Fig. 4(c)]. Since all the cavitation phenomena that we focus on occur at $x/L<0.5$, these flow phenomena associated with transition are beyond the scope of the present paper. For the present purpose, the comparison seems to indicate that the computed minimum pressure is reliable.

The cavitation inception indices of sheet cavitation (σ_i) for the three nozzles are shown in Fig. 5. They are defined as

$$\sigma_i=\frac{P_{\text{inlet}}-P_v}{0.5\rho V_{\text{inlet}}^2}, \tag{1}$$

where P_{inlet} is the pressure measured at the inlet to the test section, P_v is the vapor pressure, ρ is the density of the liquid and V_{inlet} is the velocity at the inlet. The inception indices are measured using visual observations by keeping the velocity constant and gradually reducing the pressure until cavitation appears. In the case of sheet cavitation, visual observation is straightforward. Each point is an average of several measurements that do not differ significantly. In all cases σ_i is lower than the computed $-C_{p\min}$ and there is little dependence on velocity. However, the difference between σ_i and $-C_{p\min}$ increases with increasing pressure gra-

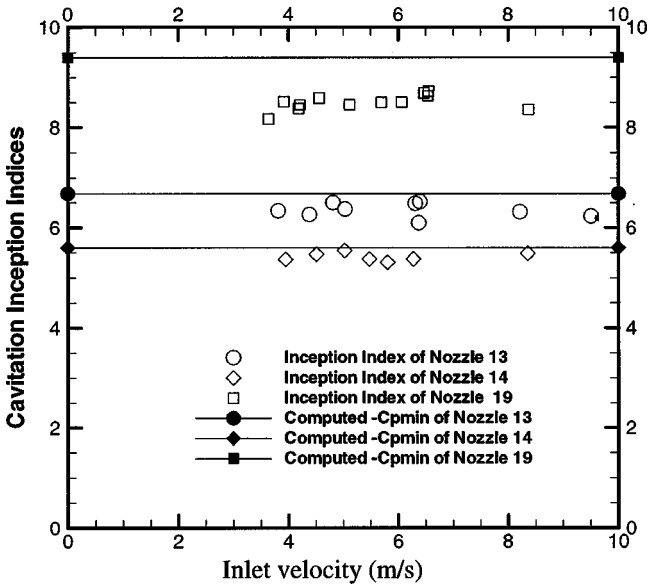

FIG. 5. Measured cavitation inception indices at different inlet velocities compared to computed minimum pressure coefficients.

dients near the minimum pressure point and can be as much as 10%. The fact that $\sigma_i = -C_{p\,\min}$ does not hold for sheet cavitation has been discussed in Refs. 46–48. However, the fact that the differences in $C_{p\,\min}$ and σ_i depend on the pressure gradients (induced by the geometry of the test object) is new. Thus, the model geometry seems to have some (but not substantial) effect on the inception indices beyond the magnitude of $-C_{p\,\min}$. The reasons for these differences are not clear, and may be related to the length of the region with pressure below the vapor pressure, which may affect both the availability of surface nuclei and the duration of exposure of free stream nuclei (in the order of 100 μsec in the present experiments). We performed tests with deaerated water (3–5 ppm) and saturated water ($\sim$15 ppm) and could not see major impact on the inception indices of ''sheet cavitation'' (which is not the case for bubble cavitation). Consistent with previous results on sheet cavitation,[49] the dissolved air content and free stream bubble distributions have insignificant effects on the inception indices. However, when the test facility contains a high concentration of ''large'' bubbles ($>$1 mm) they destroy the ''stable,'' upstream portion of the attached sheet, as reported before by Katz[4] and Ceccio and Brennen.[5]

Sample photographs of the cavitation in nozzle 13 are presented in Fig. 6. Figures 6(a) and 6(b), respectively, show the same flow conditions before and after polishing the surface of the very same nozzle. The small roughness elements of the unpolished surface are sufficient for fixing the origin of the cavitation on specific points near the minimum pressure point. Polishing the surface changes the shape of the leading edge of the cavitation to a broad and ''blunt'' pattern with a glossy leading edge. When the pressure is reduced further (to $\sigma<3$), as shown in Fig. 6(c), the glossy leading edge becomes aligned along the same axial location. The interface is still initially laminar (glossy) and is followed by a region with distinct, orderly, two-dimensional interfacial waves. These waves have been observed before by Brennen[50] on the surface of large-scale cavitation around spheres. According to Brennen, this phenomenon is a result of organized, boundary layer instability at the interface, i.e., Tollmien–Schlichting waves. After a short distance the interface becomes increasingly unstable and three-dimensional and rolls up into a series of bubbly eddies that are being shed intermittently behind the attached sheet. The relationship between the instabilities on the surface close to the leading edge and the large-scale vapor-filled cavities/structures downstream *seems* to be a process of growth of interfacial instabilities. The size and shedding frequency of these eddies on the same test object depend on the cavitation index. As already discussed in many studies, at sufficiently low cavitation indices the shedding process may involve formation of cloud cavitation (e.g., Refs. 1, 18, 20, 26, 28, and 32 and others mentioned in the Introduction). Different phases in formation of cloud cavitation in the present facility are illustrated in Fig. 6(d).

In the present paper, however, we focus on the flow structure in the closure region when the cavitation index is high enough that massive cloud shedding does not occur. Two top views are shown in Figs. 6(b) and 6(e). They both demonstrate clearly that the flow downstream of the closure region contains what appears to be hairpin-like structures containing bubbles. The transition between the continuous sheet to these hairpin structures is demonstrated in Figs. 6(f) and 6(g) in a sequence of successive images (side view) recorded at 1000 frames/sec using a high-speed digital camera (Kodak Ektapro EM Motion Analyzer, Model 1012). These images show the evolution of the same cavity (indicated by arrows) as it progresses downstream. The initially ''rounded'' mostly vapor cavity shrinks as the vapor condenses due to the local increase in pressure, tilts forward (presumably due to differences in magnitudes of the local velocities) and becomes a slender hairpin vortex with a bubbly core. This vortex is considerably taller than the vapor cavity from which it evolves and, in some cases, it reaches a height of as much as three times the height of the cavitation upstream (height of stable sheet cavity $\approx$5 mm; refer to Table I). Examinations of the high-speed movies show also that the process involves an increase in the angular velocity, i.e., as the cavity shrinks, the bubbles also start spinning at increasing speeds. Measured vorticity will be introduced later. The process repeats itself and, in fact, Fig. 6(f) also shows in the lowest frame a thicker cavity in the process of rolling up in addition to the thin hairpin vortices. In Table I we present some quantitative information obtained from the frames.

IV. FLOW STRUCTURE

A. Instantaneous flow

All the data presented in this section have been obtained with shape 13. Sample velocity and vorticity distributions at different sections along the nozzle are presented in Figs. 7(a)–7(h). As the pressure is reduced below the inception level ($\sigma=4.69$ vs $\sigma_i=6$), there are no signs of new vorticity along the stable glossy region of the interface. The veloc-

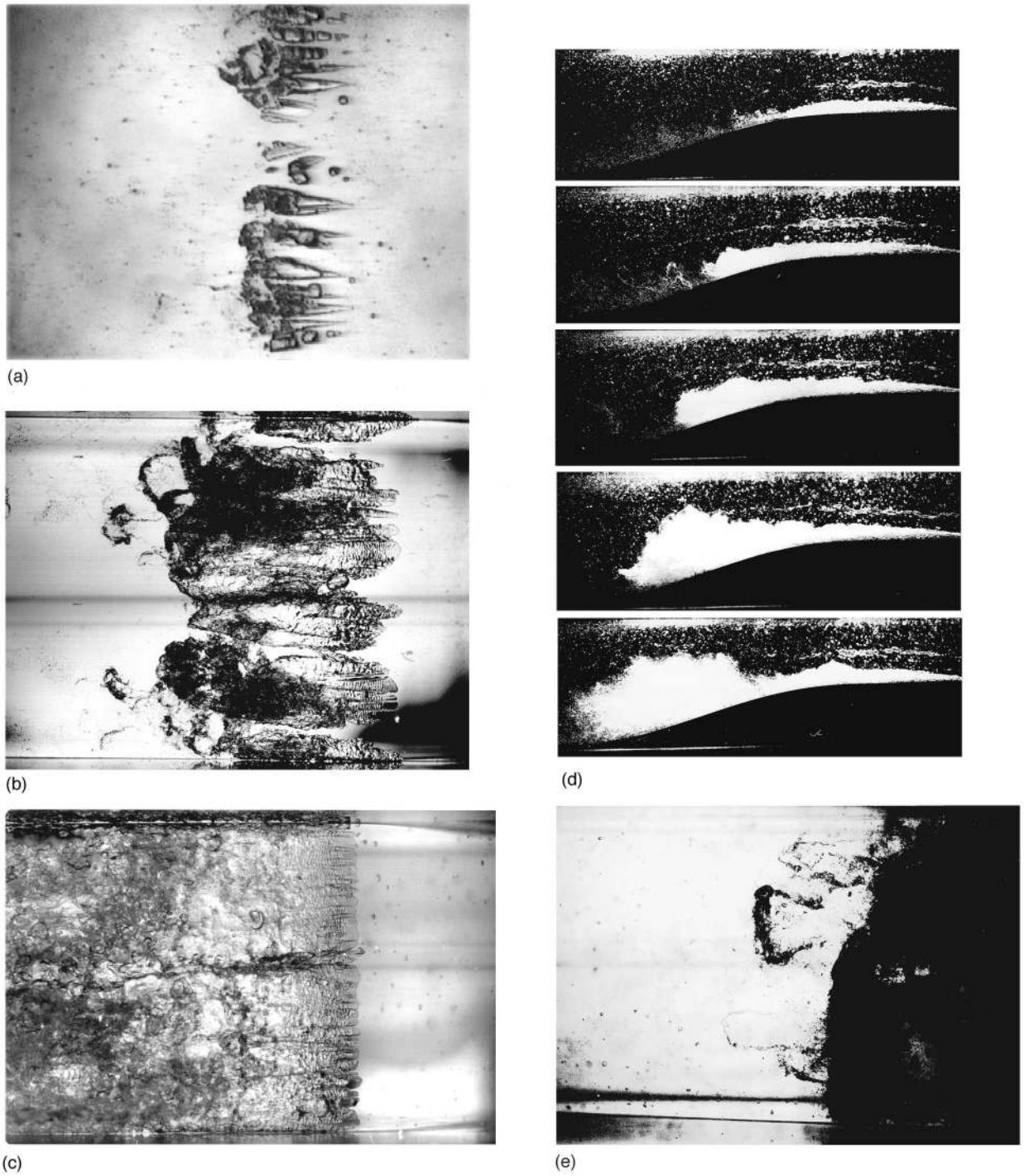

FIG. 6. Appearance of the leading edge from the top during low levels of cavitation and when the surface is (a) ''rough'' and (b) ''smooth.'' Also, note the hairpin like structures in (b), where the cavity collapses. (c) The leading edge of the sheet cavity (top view) during advanced stages of cavitation. Glassy finger-like structures are visible, which immediately become wavy. (d) Photographs (side view) showing different stages of the unsteady (advanced) cavitation phenomenon. (e) The trailing edge of the sheet cavity, as seen from the top. At least one hairpin (or horseshoe) -like structure with a bubbly core is clearly visible. (f) and (g) High-speed series of a side view. Time interval between frames is 1 msec. Note the slender structure generated after the cavity collapses. Flow is from right to left.

ity is shown in Fig. 7(a) and the vorticity is not presented, since besides two very small peaks near the interface at $x/L>0.25$ the map does not show any other phenomena (it can be found in Ref. 51). Note that the PIV interrogation window size, 1.36 mm, and the distance between windows, 0.68 mm, do not resolve the laminar boundary layer upstream of the cavitation. Signs of high vorticity peaks start appearing as the interface becomes wavy [velocity and vorticity in Figs. 7(b) and 7(c), respectively], but become quite pronounced only at the trailing edge of the cavitation [Figs. 7(d)–7(g)], i.e., at $x/L=0.35$. This region is characterized by unsteady, intermittent patches of cavities at various stages of

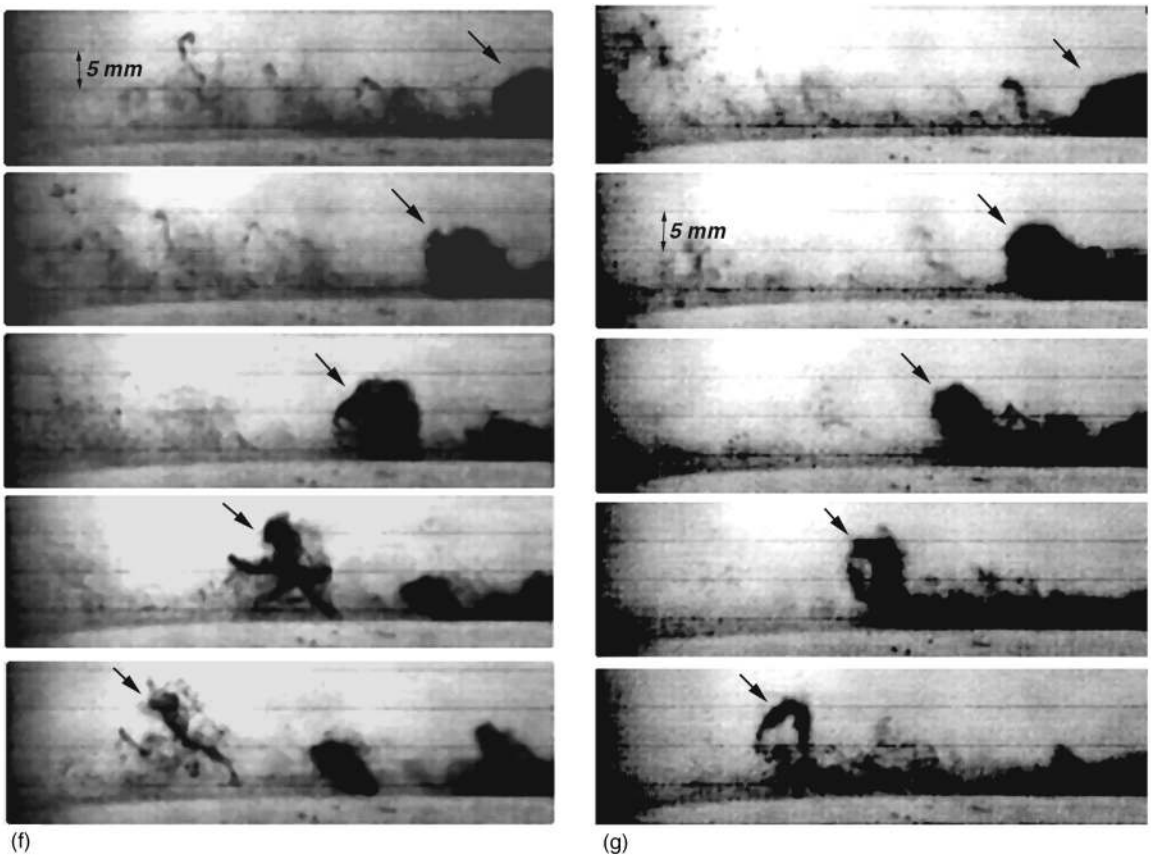

FIG. 6. (*Continued.*)

collapse as demonstrated by the three characteristic examples of the instantaneous flow. In one of the samples [Fig. 7(e)], one can even identify two inclined cavities that resemble the shapes of the vapor cavities seen in the high-speed photographs as hairpin vortices are being formed. In all cases the collapse of the cavities involves formation of high vorticity peaks of both signs, but mostly negative. Thus, the collapse of the vapor cavities involves substantial vorticity production in the closure region of the sheet cavity. The large eddies generated in this region are convected downstream without evidence of additional significant level of vorticity production. In Fig. 7(h) that covers the region upstream of the fully wetted boundary layer transition [see Fig. 4(d)]. The eddies reach elevation of almost three times the height of the sheet cavity—consistent with the photographs shown in Figs. 6(f) and 6(g).

TABLE I. Data from high speed frames [Figs. 6(f) and 6(g)].

	Height of cavity/structure (mm)		Convection speed of cavity/structure (m/sec)	
Frame No.	Figure 6(f)	Figure 6(g)	Figure 6(f)	Figure 6(g)
1	8.6	8		
2	9	10.3	8.3	
3	10.4	10.9	10.6	10.6
4	13.2	11.8	12	10.6
5	14.3	12.9	13	11

To summarize the process, the PIV data and the photographs show that as the water vapor interface becomes wavy and condensation starts, portions of the cavitation become detached. These odd-shaped, mostly vapor, cavities are convected briefly downstream but condense quickly (within about 2 msec), creating in the process powerful vortices. As the sample velocity distributions in the closure region demonstrate [Figs. 7(a), 7(b), and 7(d)], under the present flow conditions, i.e., just below inception with cavity height of about 3 mm, there is no reverse flow even very close to the wall at the trailing edge of the cavitation. This conclusion is based on careful examination of all the PIV images of the flow in the closure region (a total of 120 instantaneous vector maps, as will be discussed shortly). To confirm this conclusion we have also checked the traces of individual particles very close to the wall in a few images to examine whether there is reverse flow at scales smaller than the interrogation window. We have seen no evidence of reverse flow. *There is no reentrant flow under the present flow conditions*. The ''large'' vapor cavities simply shrink as the vapor condenses and the horizontal velocity around them remains positive. This observation is not consistent with the typical reentrant flow model for the closure region of attached cavitation. It agrees, however, with a comment made in a recent paper by Callenaere *et al.*[32] that when the cavities are thin, the adverse pressure gradients may be too weak for creating a reentrant jet. Note also that we do not claim here that there is no reverse flow under more developed states of cavitation. In

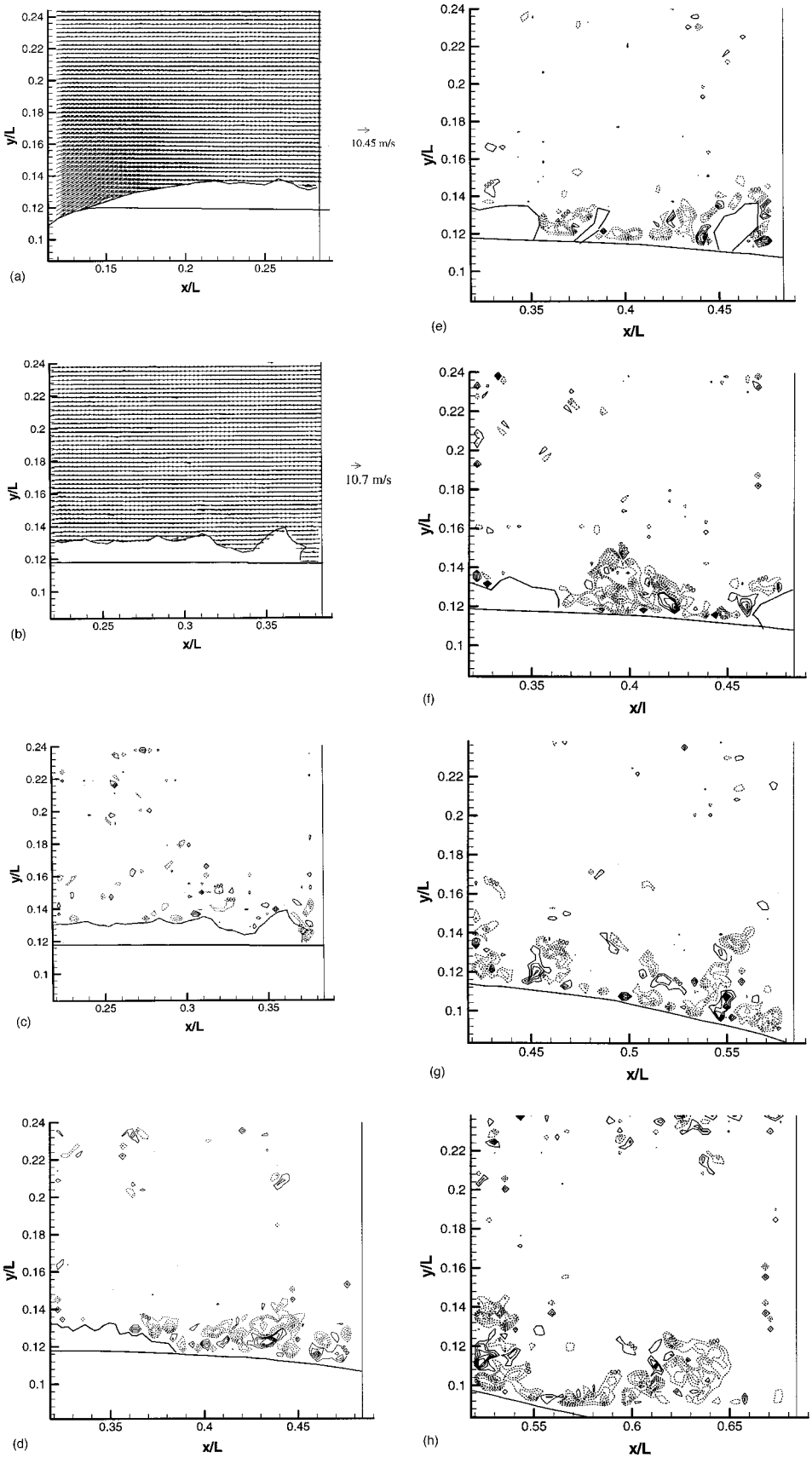

FIG. 7. (a) Sample instantaneous velocity map at the leading edge of the cavity for σ=4.69. (b) and (c) show velocity and vorticity slightly downstream. (d)–(h) all show instantaneous vorticity at various axial locations. Increment in contour lines is 500 l/sec. Dotted lines represent negative vorticity, i.e., clockwise rotation.

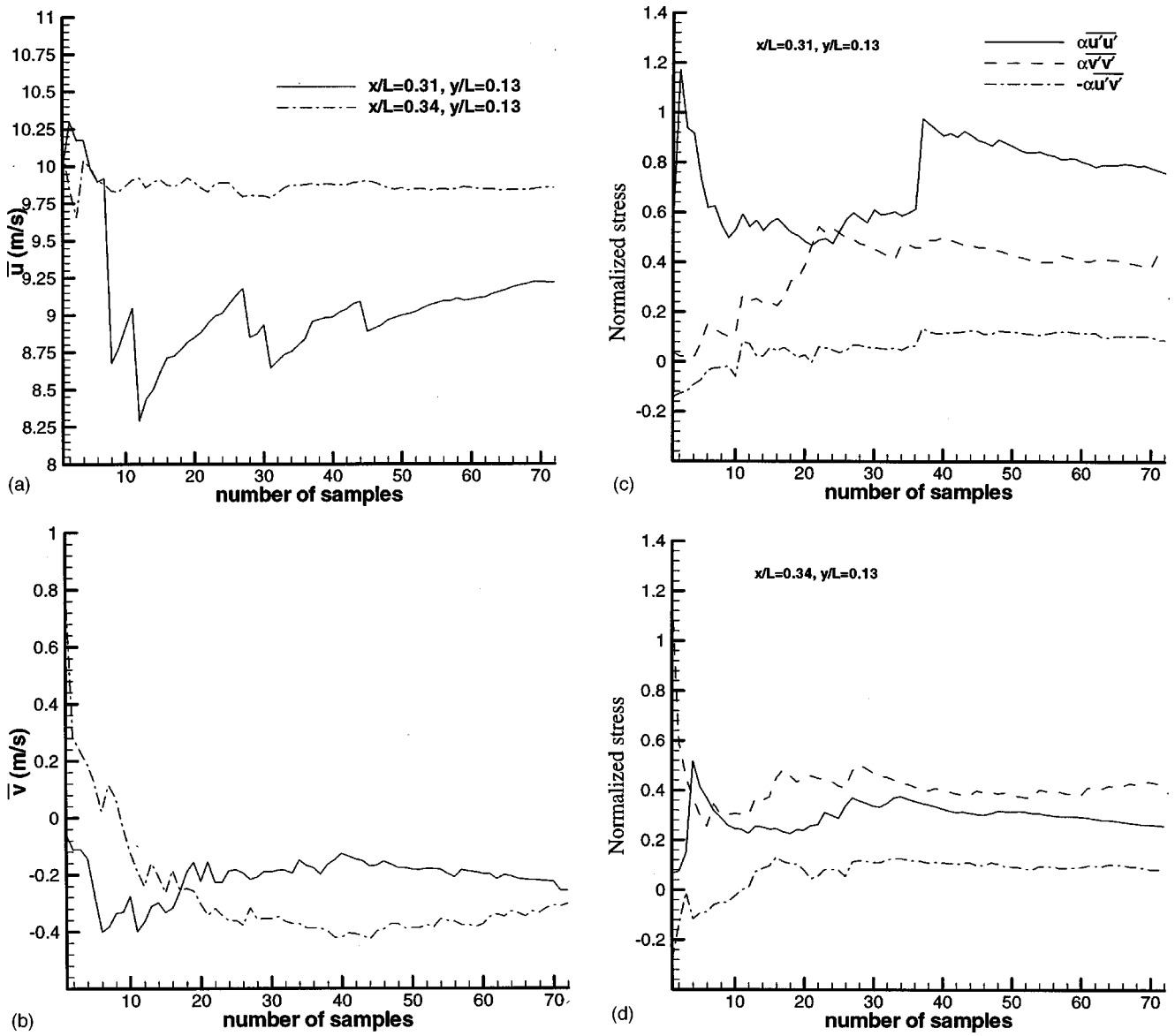

FIG. 8. Running average of (a) horizontal velocity, (b) vertical velocity, and (c) and (d) normalized stresses at random sample points to illustrate convergence of data. Turbulence level is maximum at $x/L=0.31$ and significantly drops at $x/L=0.34$.

fact, intermittent reverse flow occurs under the giant bubbly vortices that are being shed behind the closure region, even in the present facility, but only during advanced stages of cloud cavitation (much lower σ). From observations so far, we say that an adverse pressure gradient is a necessary condition for the formation of a reentrant flow. The question remains as to the magnitude of the adverse pressure gradient that would cause the reentrant flow. There can be two reasons for an adverse pressure gradient—(a) induced by the geometry of test object and (b) caused by the cavitation [pressure downstream of cavitation is higher than P_v, Fig. 19(a)]. In our experiments in the region $0.2<x/L<0.3$, (a) is very mild and (b) is clearly dominant. If the cavitation is extended (by lowering σ) to $x/L=0.4$, we see reverse flow because of the strong geometry-induced adverse pressure gradient (Fig. 3) in addition to the one already caused by the cavitation. We have not made any systematic study of these trends. However, increased likelihood of reverse flow under the cavitation with increasing adverse pressure gradients along the wall prior to the onset of cavitation is consistent with the observations of Callenaere *et al.*[32] This advanced level of cavitation is not in the scope of the present study.

B. Mean flow and void fraction distributions

Two data series, both at the same velocity and pressure, but at different water temperatures, 35 °C and 45 °C, have been recorded. They provide essentially the same hydrodynamic conditions with $V_{\text{inlet}}=5.2$ m/sec (the effect on viscosity is negligible), but the resulting cavitation indices, 4.69 and 4.41, respectively, vary slightly due to the different vapor pressure. This slight change has a strong impact on the extent of cavitation, flow structure and turbulence. Trends in cavity length as a function of the cavitation index σ (usually scales as $1/\sigma$) are examined in Ref. 16. We analyzed 72 images at $\sigma=4.69$ and 48 PIV images at $\sigma=4.41$. Running

averages of velocity components and Reynolds stress for $\sigma=4.69$ are shown in Fig. 8. The data show that convergence is reasonably achieved. Due to the presence of bubbles along the walls, each image had to be examined carefully to remove the bubble traces before computing the velocity distributions (although the laser wavelength was filtered, there is some secondary reflection of fluorescent light from the surface of the bubbles). Otherwise, the bubbles contaminated the liquid velocity measurements. As discussed before, the length of the cavities varied from one image to the next and odd-shaped detached patches appeared frequently. Still, it was evident that the height and length of the cavitation increase substantially with the small change in σ.

When one attempts to determine the ensemble average of the flow in the closure region, the averaging process should take into account the existence of two phases with nonuniform spatial distributions and the phase change. The ensemble-averaged continuity equation for the liquid is

$$\frac{\partial(\alpha_l\overline{\rho_l})}{\partial t}+\frac{\partial(\alpha_l\overline{\rho_l u_{li}})}{\partial x_i}=\left[\frac{D\alpha_v\overline{\rho_v}}{Dt}\right], \tag{2}$$

where over-bar indicates ensemble average, the subscripts l and v refer to liquid and vapor, respectively, and α_i is the void fraction, i.e. the fraction of observations (images) for which a certain interrogation window contains the phase i. Note that $\alpha_l=1$ corresponds to $\alpha_v=0$. A ''phasic indicator'' was used on each image and vapor/voids were given a value of 0, and liquid were given a value of 1. Then an ensemble average was obtained (from 72 images for $\sigma=4.69$ and 48 for $\sigma=4.41$; thus, data at $\sigma=4.69$ is more reliable), providing the distribution of α_l. In principle it is possible that ''holes'' could show up on PIV images from bubbles that are not in the light sheet plane but between the sheet and camera. This is not the case in the present data since the cavities are small compared to the size of the camera lens that is located quite close to the light sheet. Thus, out-of-plane cavities do not block details in the light sheet plane. Equation (2) brings into account that the only source of mass for the liquid is condensation of the vapor phase. Assuming that the mean flow is steady and that the liquid density is constant,

$$\frac{\partial(\alpha_l\overline{u_i})}{\partial x_i}=-\frac{\partial(\alpha_v(\rho_v/\rho_l)\overline{u_{vi}})}{\partial x_i}. \tag{3}$$

Due to the substantial differences in density, the source term on the right-hand side is negligible and, assuming that the averaged flow is two-dimensional, the continuity equation becomes

$$\frac{\partial(\alpha_l\overline{u}_l)}{\partial x}+\frac{\partial(\alpha_l\overline{v}_l)}{\partial y}=0. \tag{4}$$

Distributions of α_l, $\overline{u_l}$ and $\alpha_l\overline{u_l}$ for $\sigma=4.69$, $\overline{u_l}$ and $\alpha_l\overline{u_l}$ for $\sigma=4.41$, $\overline{v_l}$ and $\alpha_l\overline{v_l}$ for $\sigma=4.69$ and $\overline{v_l}$ and $\alpha_l\overline{v_l}$ for $\sigma=4.41$ are presented in Figs. 9–13, respectively. As Fig. 9 shows, in both cases α_l gradually increases from zero to one, but the dimensions of the cavitating region increase substantially with the slight decrease in σ. This trend is evident for all the values of void fraction, but especially for the $\alpha_l=0.1$ and 0.2

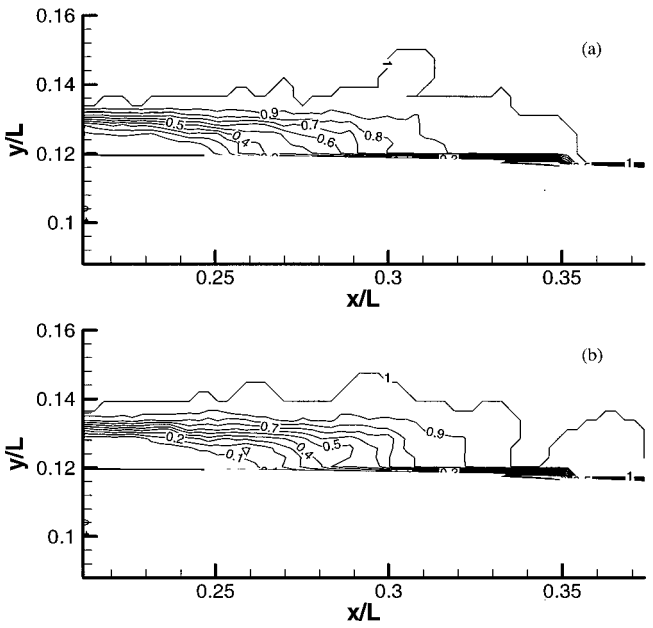

FIG. 9. Measured distributions of void fraction (α_l) for (a) $\sigma=4.69$ and (b) $\sigma=4.41$. Increment in contour lines is 0.1.

lines. Also, the vertical and horizontal gradients in α_l increase with decreasing σ. Thus, while attempting to model the void fraction distributions, the expressions that come to mind are in the form of

$$\alpha_l(\sigma-\sigma_i,C_p)=1-\exp\left[-K_x\left(\frac{x-x_{\text{ref}}}{h_{\text{cav}}}\right)^{n_x}-K_y\left(\frac{y-y_0}{h_{\text{cav}}}\right)^{n_y}\right], \tag{5}$$

where K_i and n_i are coefficients, h_{cav} is the height of the cavity, x_{ref} is a reference location (such as the location of the maximum height of the cavitation) and y_0 is the wall elevation. All these coefficients are functions of $(\sigma-\sigma_i)$ and the pressure coefficient in the closure region. In the present paper we present only examples of the effect of $\sigma-\sigma_i$, but other studies, such as Ref. 32, demonstrate also the substantial effect of the pressure gradients on the flow structure and cavitation in the closure region (including the formation of a reentrant jet). In the present flow conditions $\partial C_p/\partial x\sim 0$. x_{ref} can be chosen as the location of the transition between stable to intermittent shedding/collapse of the cavitation. Besides being a function of $\sigma-\sigma_i$ and pressure gradients, since the interface stability is affected by the Reynolds number,[50] α_l is probably also a function of the Reynolds number. Since we did not determine the distribution of α_l for many conditions, we cannot report on trends. However, for the present data at $\sigma=4.69$, $n_x=2.07$, $n_y=2.6$, $K_x=0.027$ and $K_x=1.24$. This distribution is shown in Fig. 14. The relative rms difference between this curve and the experimental data [Fig. 9(a)] in the region between the wall and $y/L=0.14$, $0.215<x/L<0.36$, is 4%.

Another feature of the closure region can be observed in the distributions of vertical velocity (Figs. 12 and 13). Above the immediate vicinity of the wall (1–2 mm) and all around the cavity in the closure region, the vertical velocity is negative, a trend associated with the flow surrounding the cavita-

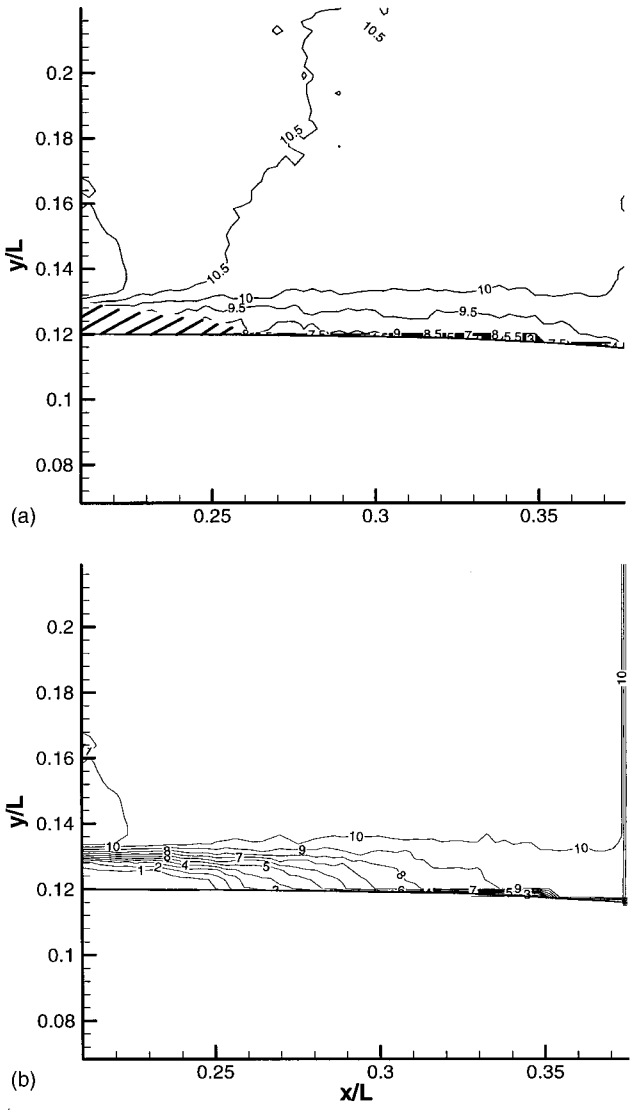

FIG. 10. Distributions of (a) $\bar{u}$ and (b) $\alpha_l \bar{u}$ for the case $\sigma=4.69$. Hatched zone represents the region where points have less than 20 measurements, i.e., liquid velocity.

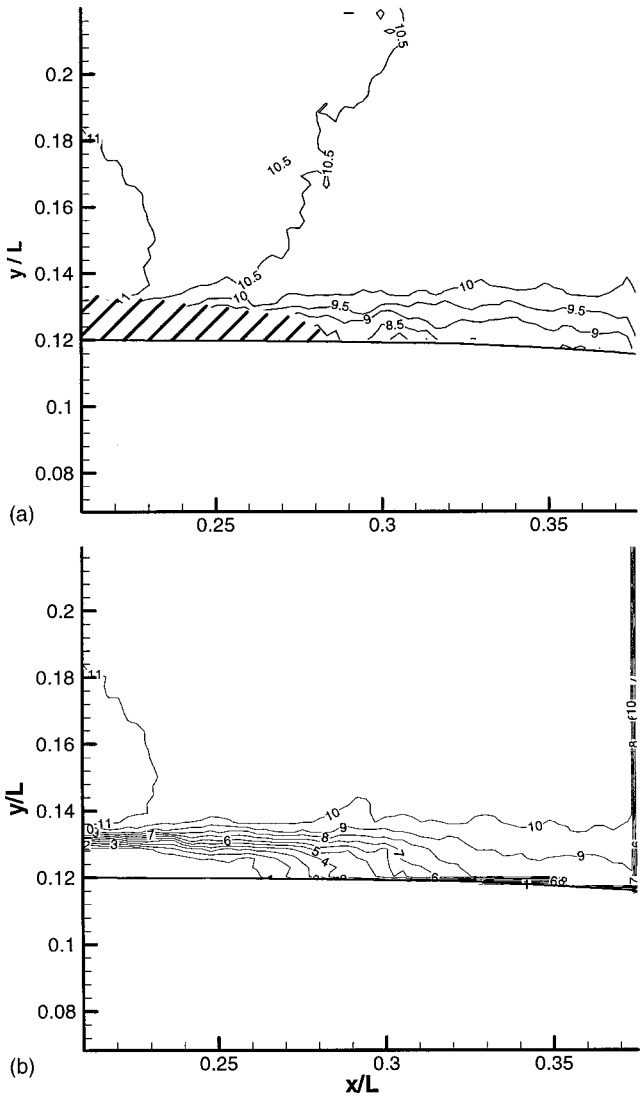

FIG. 11. Distributions of (a) $\bar{u}$ and (b) $\alpha_l \bar{u}$ for the case $\sigma=4.41$. Hatched zone represents the region where points have less than 20 measurements, i.e., liquid velocity.

tion. For both the cavitation indices $\overline{v_l}$ and $\alpha_l \overline{v_l}$ are positive very close to the wall. Examination of the instantaneous velocity distributions in this region shows that this phenomenon is caused by the collapse of the vapor cavities and the generation of large vortices. Sample close-up velocity and vorticity maps demonstrating this are presented in Fig. 15. They show that the vertical velocity is positive on both sides of the collapsing vapor cavities. The upward motion of the lower cavity wall contributes to this positive motion below the cavity. The vortical motion that develops as a result of the cavity collapse [Fig. 15(b)] causes the positive vertical velocity above the cavity.

V. MODELING ISSUES

A. Mass balance

Due to the sharp gradients in α_l, as expected, the high gradients in vertical velocity ($\partial \bar{v}_l/\partial y<0$, Fig. 12) are not balanced by $\partial \bar{u}_l/\partial x>0$ (Fig. 10) of the same magnitude. Clearly, the average liquid velocity distributions, by themselves, do not satisfy the two-dimensional incompressible flow continuity equation. In fact, in some cases both gradients have the same sign. On the other hand, the values of $\partial \alpha_l \overline{v_l}/\partial y<0$ are matched by the proper values of $\partial \alpha_l \overline{u_l}/\partial x>0$, satisfying Eq. (4). To illustrate this conclusion, Fig. 16 shows the distribution of η and η_α, defined as

$$\eta=\frac{(\partial \bar{u}_l/\partial x+\partial \overline{v_l}/\partial y)^2}{(\partial \overline{u_l}/\partial x)^2+(\partial \bar{v}_l/\partial y)^2};$$
$$\eta_\alpha=\frac{(\partial \alpha_l \bar{u}_l/\partial x+\partial \alpha_l \overline{v_l}/\partial y)^2}{(\partial \alpha_l \bar{u}_l/\partial x)^2+(\partial \alpha_l \bar{v}_l/\partial y)^2}. \tag{6}$$

These distributions are obtained in the two-phase region, viz. $0.23<x/L<0.3$, $0.118<y/L<0.14$, for $\sigma=4.69$, hence obtained from 72 instantaneous realizations. Note that distributions of $\overline{u_l}$, $\overline{v_l}$, $\alpha_l \overline{u_l}$, $\alpha_l \overline{v_l}$ are presented in Figs. 10 and 12, respectively. We did not compute η and η_α for $\sigma=4.41$. The quantity η equals 0 when the continuity equation is satisfied

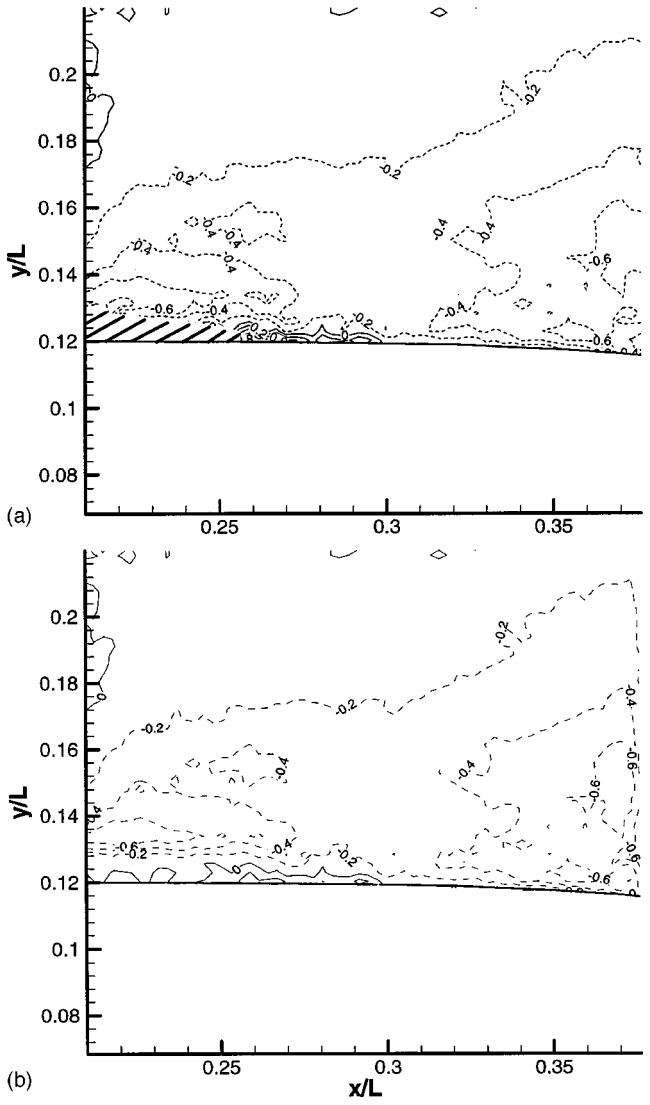

FIG. 12. Distributions of (a) $\bar{v}$ and (b) $\alpha_l \bar{v}$ for the case $\sigma=4.69$. Dashed lines represent negative quantity.

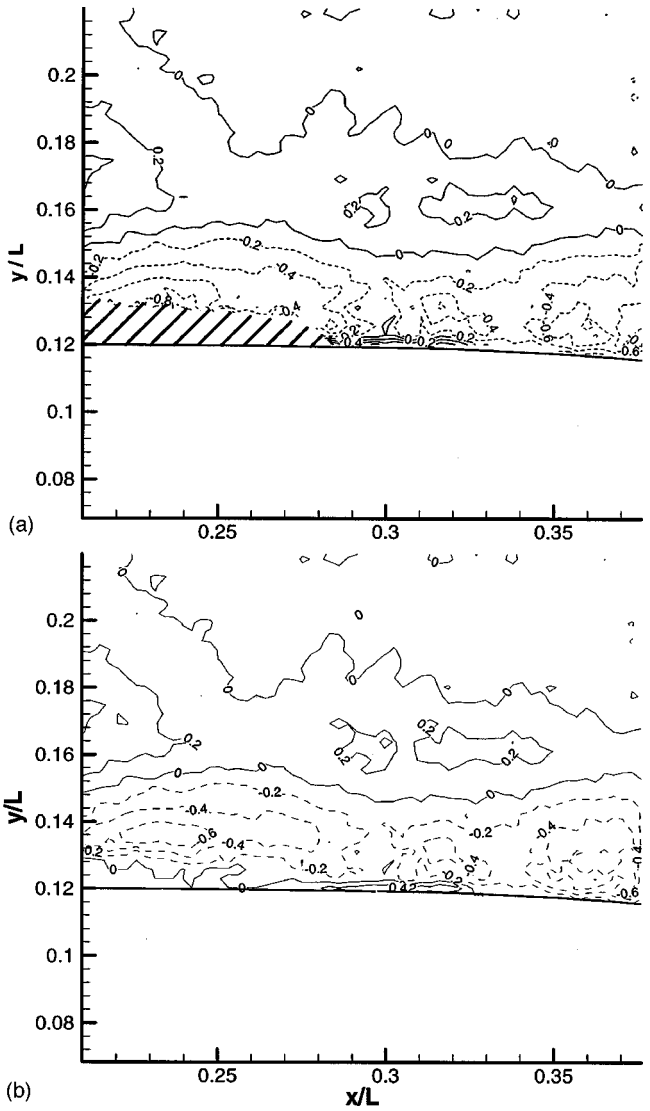

FIG. 13. Distributions of (a) $\bar{v}$ and (b) $\alpha_l \bar{v}$ for the case $\sigma=4.41$. Dashed lines represent negative quantity.

and is larger than 1 when both velocity gradients have the same sign. The average value of η is 1 when u and v are random, unrelated numbers.[52] The results clearly show that introducing the void fraction causes a substantial drop in the number of cases with values equal to or greater than 1, and an increase in the number of cases with values less than 0.25. Clearly, the closure region must be treated as a two-phase flow.

B. Reynolds stresses, momentum balance and interaction terms

The Reynolds averaged momentum equations for the liquid phase, neglecting the viscous terms, can be written as (from Ref. 53)

$$\frac{\partial(\alpha_l \bar{u}_l \bar{u}_l)}{\partial x} + \frac{\partial(\alpha_l \bar{u}_l \bar{v}_l)}{\partial y} = -\frac{1}{\rho}\frac{\partial \alpha_l \bar{p}}{\partial x} - \frac{\partial(\alpha_l \overline{u_l' u_l'})}{\partial x} - \frac{\partial(\alpha_l \overline{u_l' v_l'})}{\partial y} + M_x, \tag{7}$$

$$\frac{\partial(\alpha_l \bar{u}_l \bar{v}_l)}{\partial x} + \frac{\partial(\alpha_l \bar{v}_l \bar{v}_l)}{\partial y} = -\frac{1}{\rho}\frac{\partial \alpha_l \bar{p}}{\partial y} - \frac{\partial(\alpha_l \overline{u_l' v_l'})}{\partial x} - \frac{\partial(\alpha_l \overline{v_l' v_l'})}{\partial y} + M_y - g, \tag{8}$$

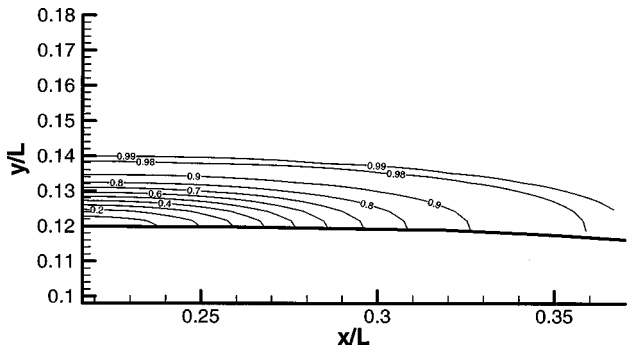

FIG. 14. Empirical distribution of the void fraction for $\sigma=4.69$, using Eq. (5). The coefficients are $n_x=2.07$, $n_y=2.6$, $K_x=0.027$and $K_y=1.24$.

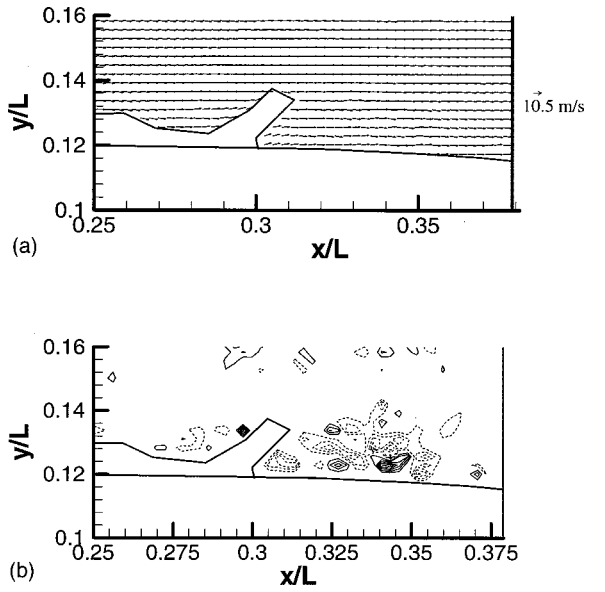

FIG. 15. Sample close-up of (a) velocity and (b) vorticity during cavity collapse. First contour level is ±500 l/sec (dashed lines represent negative vorticity) and increments are of 500 l/sec.

where M_i is the interaction term, i.e., the effect of the vapor phase on the momentum of the liquid phase. Distributions of normal stresses $\alpha_l \overline{u_l' u_l'}$, $\alpha_l \overline{v_l' v_l'}$ and shear stress $\alpha_l \overline{u_l' v_l'}$ and the estimated turbulent kinetic energy $\alpha_l k^* = 0.75(\alpha_l \overline{u_l' u_l'} + \alpha_l \overline{v_l' v_l'})$ (it is based on the assumption that the third component is the average of the two measured components) for $\sigma = 4.69$ are presented in Fig. 17 (note the multiplicative constants). Although the number of samples for $\sigma = 4.41$ is smaller (48 as compared to 72 for $\sigma = 4.69$), we present the turbulent kinetic energy (Fig. 18) to demonstrate the effect of a lower σ. As seen in the figures, along the wall the turbulence level increases considerably with the slight decrease in σ. The peaks in $\alpha_l k^*$ more than double and their locations

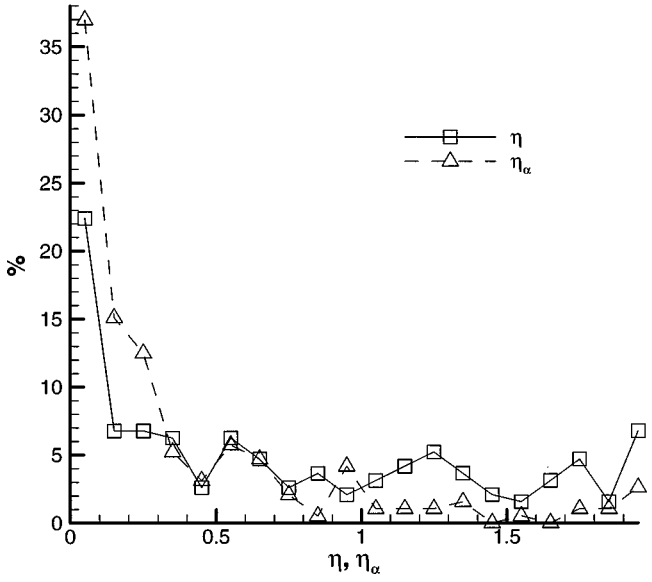

FIG. 16. Distributions of η and η_α [Eq. (6)], illustrating the effect of void fraction on the continuity equation.

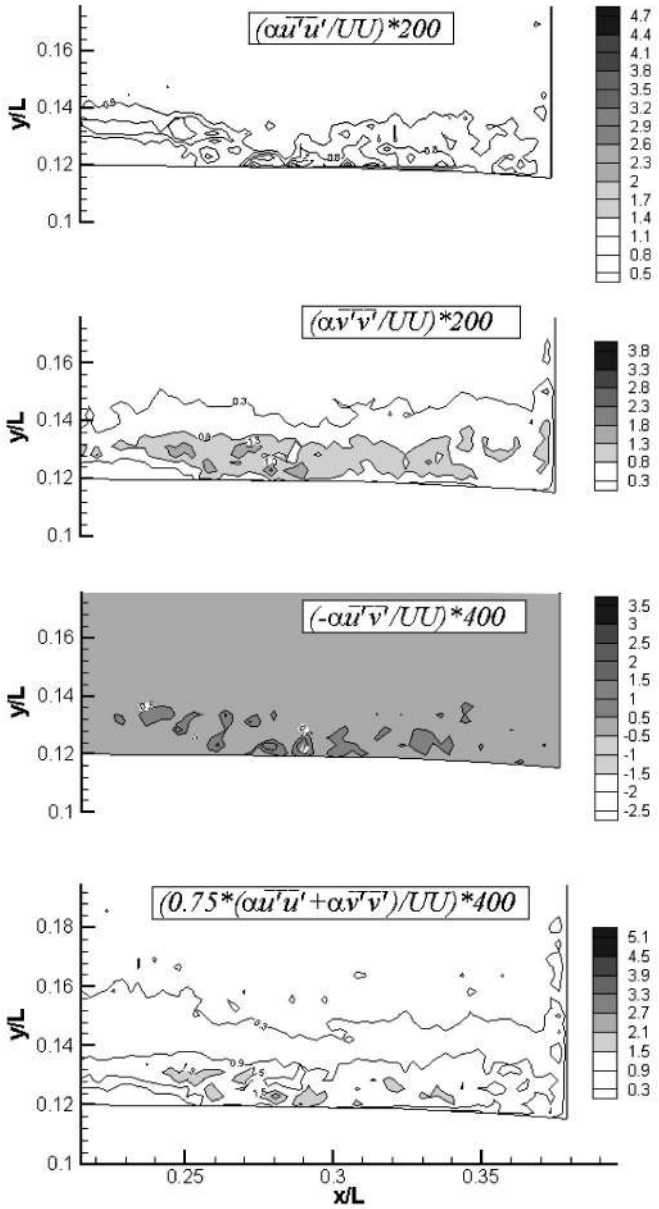

FIG. 17. Distributions of (a) and (b) normal Reynolds stresses, (c) shear stress, and (d) turbulent kinetic energy for $\sigma = 4.69$.

shift downstream. Note that the highest velocity fluctuations actually occur upstream of the regions indicated in Figs. 17 and 18, but their impacts are diminished by the multiplication with the void fraction (Fig. 9). Interestingly, above the cavitation, namely at $x/L < 0.27$ and away from the wall, the effect of σ is relatively small, i.e., in both cases $\alpha_l k^*$ have similar magnitudes. Also the data at $\sigma = 4.69$ show that $\alpha_l \overline{u_l' u'}_l$ and $\alpha_l \overline{v_l' v'}_l$ have comparable magnitudes. The peaks in $-\alpha_l \overline{u_l' v_l'}$ are about 25%–40% of the $\alpha_l k^*$ peaks, a ratio that characterizes separated flows with large coherent structures, consistent with the instantaneous distributions. Note that these levels are significantly higher than velocity fluctuations in turbulent boundary layers,[54] but are comparable to peak levels within a separated region, for example, behind backward-facing steps.[55]

It is also important to determine the effect of the inter-

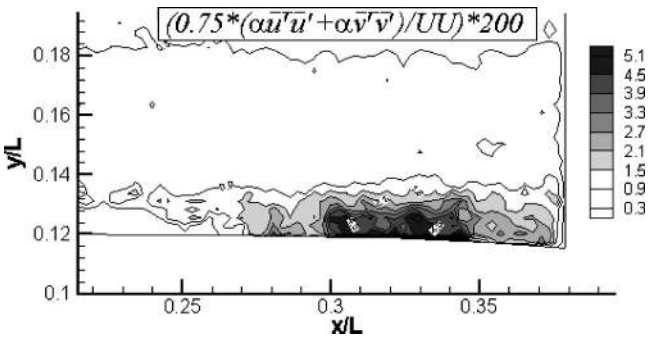

FIG. 18. Distribution of turbulent kinetic energy for $\sigma=4.41$.

action terms. Since we cannot determine the magnitude of M_i directly, one needs to evaluate the rest of the terms in the momentum equation and determine whether the interaction terms contribute substantially to the overall liquid momentum. A troublesome term is the pressure gradient. It is not clear to us that the streamwise pressure distribution in the closure region satisfies the boundary layer assumption, i.e., that the pressure is predominantly a function of x only. To partially answer this question, one can look at the pressure distribution above the cavitation, where the turbulent terms are negligible and $\alpha_l=1$. Consequently, the horizontal and vertical pressure gradients can be determined from the acceleration terms only. Pressure gradient distributions at different elevations, estimated from the values of $-(\bar{u}_l\partial\bar{u}_l/\partial x+\bar{v}_l\partial\bar{u}_l/\partial y)$ and $-(\bar{u}_l\partial\bar{v}_l/\partial x+\bar{v}_l\partial\bar{v}_l/\partial y)-g$, are presented in Fig. 19. Here the pressure is scaled with U^2/L, where $U=10.5$ m/sec is the velocity in the undisturbed region above the cavitation ($U^2/L=441$ m/sec^2 or 45 g). It is clear that $\partial p/\partial x$ varies significantly with y, as one would expect, considering that the pressure near the cavity interface should be close to vapor pressure. Thus, the *best* that we can do with the present data is to choose the pressure as close as possible to the cavitation interface, where the liquid void fraction is still one, i.e., $y/L=0.14$. Note that near the closure region of the cavitation there are substantial adverse pressure gradients that do not exist in the noncavitating flow (compare to Fig. 3).

Interestingly, since we measure the pressure at the entrance to the test section (to determine σ), where the $u_l=5.2$ m/sec, we can use the Bernoulli equation to estimate the pressure at any point in the test section as long as viscous/turbulence effects are not important. Using this approach one can determine, for example, that the absolute pressure at $x/L=0.215$, $y/L=0.215$, where the velocity is almost uniform and $\partial p/\partial y\approx 0$, is 1.64×10^4 Pa over the vapor pressure. Then, vertical integration using the measured values of $\partial p/\partial y$ (Fig. 19) leads to a pressure of approximately 5000 Pa over vapor pressure at $y/L=0.132$, $x/L=0.215$. This result also shows the validity of our measurements since this point is located near the cavitation interface and hence the pressure should be close to P_v. Once the local pressure can be evaluated, $\partial(\alpha_l p)/\partial x$ and $\partial(\alpha_l p)/\partial y$ can be computed at every point along $y/L=0.132$.

Thus, using the pressure gradients at $y/L=0.14$, the terms in the momentum equations are now available and we

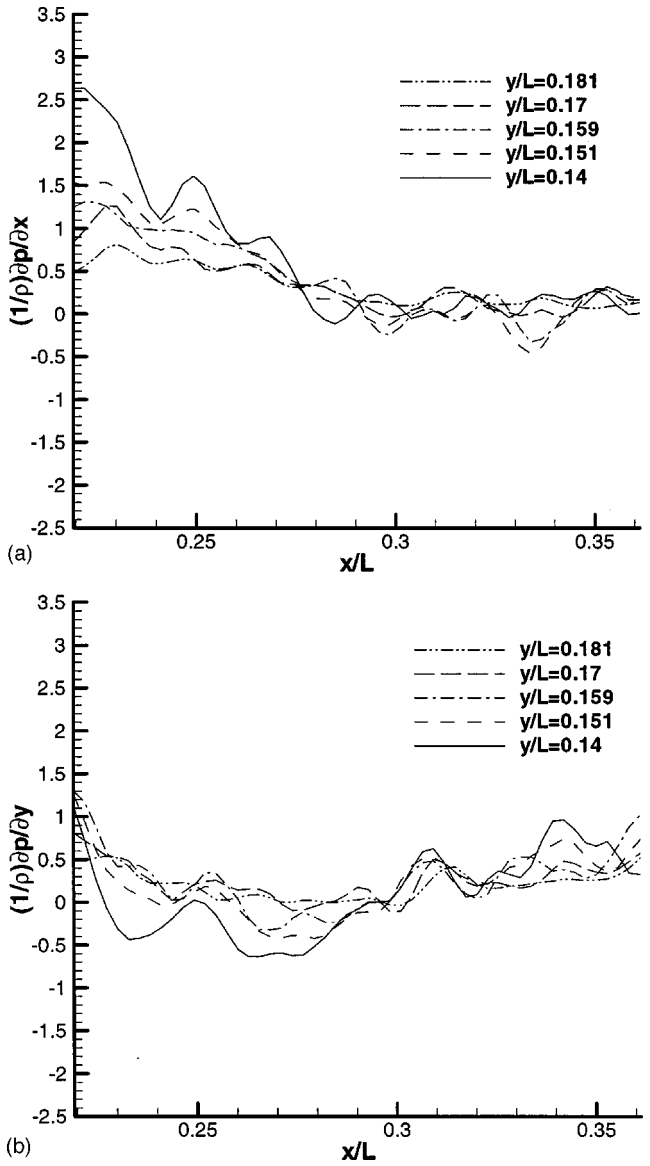

FIG. 19. Distributions of (a) $(1/\rho)\partial p/\partial x$ and (b) $(1/\rho)\partial p/\partial y$ at several elevations. The quantities are normalized by $U^2/L(=45$ g).

can substitute them in order to estimate the interaction terms. In order to reduce the jitter associated with the derivatives, the vectors are spatially filtered prior to differentiation. A simple ''box filter'' is used, i.e., each velocity vector is replaced with an average of the 4×4 neighboring vectors. Again, all the results are scaled with U^2/L (=45 g) and are summarized in Figs. 20 and 21. In the horizontal momentum balance the turbulent stresses have little impact on the results. The dominant terms are clearly the pressure gradients and $\alpha_l u_l\partial u_l/\partial x$, but $\alpha_l v_l\partial u_l/\partial y$ is not negligible. M_x is significantly smaller than the convective terms and pressure gradients except for $x/L<0.23$, where it becomes negative. In this region, due to the proximity to $\alpha=0$, we suspect that there are significant differences between $\partial p/\partial x|_{y/L=0.132}$ and $\partial p/\partial x|_{y/L=0.14}$ [evident in Fig. 19(a), where the gradients begin to vary considerably as the cavity is approached), which may cause this deviation from zero. Conversely, in the vertical pressure gradients [Fig. 19(b)] the changes with el-

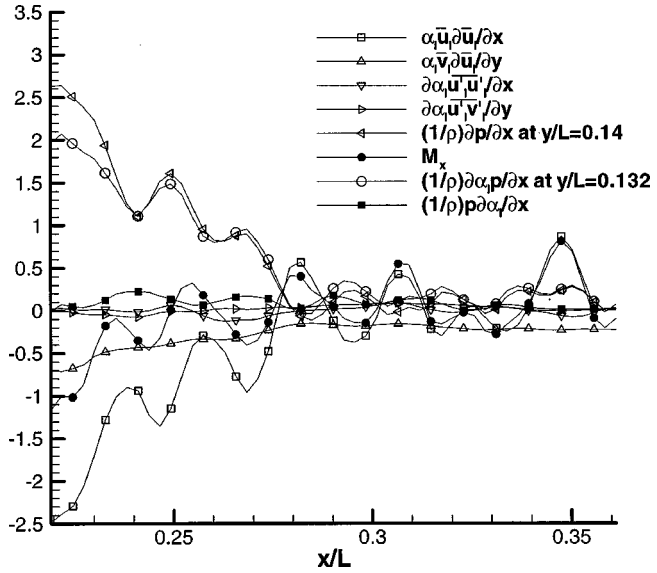

FIG. 20. Terms of the horizonal momentum balance [Eq. (7)]. M_x is the interaction term. Quantities are normalized by $U^2/L(=45\ \mathrm{g})$.

evation are small, yielding more reliable results for the vertical momentum equation.

All the terms in the vertical momentum equation are small compared to the horizontal terms except for $\partial(\alpha_l p)/\partial y$. This term is large for a significant fraction of the closure region due to the large vertical gradients in α_l (Fig. 9), leading to a high interaction term in the y direction. Since $\alpha_l \partial p/\partial y$ is small, ρM_y is essentially equal to $p\partial\alpha_l/\partial y$, very clearly seen in Fig. 21.

In the equations derived by Drew and Lahey[53] for flows without phase change, the expression for M_i is

$$\rho M_i = p\frac{\partial \alpha_l}{\partial x_i} - \tau_{ij}\frac{\partial \alpha_l}{\partial x_j} + M_i', \tag{9}$$

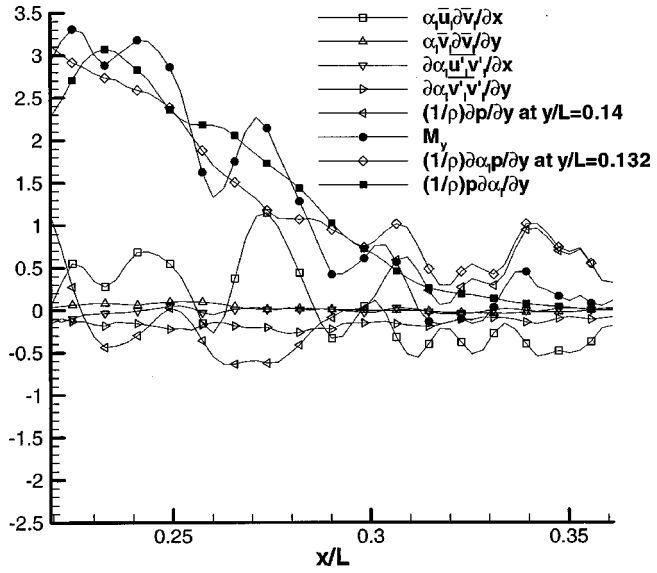

FIG. 21. Terms of the vertical momentum balance [Eq. (8)]. M_y is the interaction term. Quantities are normalized by $U^2/L(=45\ \mathrm{g})$.

where τ_{ij} is the viscous stress and M_i' is a fluctuating term resulting from ensemble averaging. In the present measurements, both the viscous stresses and the fluctuating terms are small (e.g., see the effect of Reynolds stresses on the balance) compared to the convective terms and pressure gradients, resulting in

$$\rho M_i \approx p\frac{\partial \alpha_l}{\alpha x_i}. \tag{10}$$

Thus, at least for the present low levels of cavitation, the interaction term is equal to the pressure multiplied by the gradients of the void fraction. Consequently, in order to analyze the flow in the closure region one can solve the following momentum equation,

$$\alpha_l \bar{u}_{lj}\frac{\partial \bar{u}_{li}}{\partial x_j} = -\frac{\alpha_l}{\rho}\frac{\partial \bar{p}}{\partial x_i} - \frac{\partial(\alpha_l \overline{u'_{li}u'_{lj}})}{\partial x_j}. \tag{11}$$

Since, for the existing conditions, the gradients of the Reynolds stresses are still substantially smaller than the other terms, α_l may be canceled and Eq. (11) can be reduced to a simple ''Euler equation'' for the liquid velocity. Note that this conclusion is appropriate only for conditions where the stress gradients (viscous and Reynolds) are small. However, α_l still remains in the continuity equation.

C. Momentum and displacement thickness

Finally, for boundary layer modeling, it is of interest to determine the effect of cavitation on the momentum thickness θ, $\alpha_l\theta$ and the displacement thickness, δ^*, $\alpha_l\delta^*$. They are defined as

$$\begin{aligned}
\theta &= \sum_{\text{wall}}^{y/L=0.19} \frac{u}{u_{y/L=0.19}}\left(1-\frac{u}{u_{y/L=0.19}}\right)\Delta y,\\
\delta^* &= \sum_{\text{wall}}^{y/L=0.19} \left(1-\frac{u}{u_{y/L=0.19}}\right)\Delta y,\\
\alpha_l\theta &= \sum_{\text{wall}}^{y/L=0.19} \frac{\alpha_l u}{u_{y/L=0.19}}\left(1-\frac{u}{u_{y/L=0.19}}\right)\Delta y,\\
\alpha_l\delta^* &= \sum_{\text{wall}}^{y/L=0.19} \alpha_l\left(1-\frac{u}{u_{y/L=0.19}}\right)\Delta y.
\end{aligned} \tag{12}$$

Distributions of θ, $\alpha_l\theta$, δ^* and $\alpha_l\delta^*$ are presented in Fig. 22. Note that the integral momentum equation would include the terms multiplied by α_l. It is clear that the turbulence generated by the collapse of the cavitation causes a substantial increase in the momentum deficit near the boundary. Upstream of (or in the absence of) the cavitation, the entire boundary layer thickness is smaller than our vector spacing of 0.675 mm. Also, the slight change in the cavitation index increases (almost doubles) the magnitude and extends the horizontal length of the region with high momentum and displacement thickness. Both $\alpha_l\theta$ and $\alpha_l\delta^*$ decrease as the void fraction recovers to 1.0, but their magnitudes remain substantially higher than any value that exists in the boundary layer upstream of the cavitation. The momentum deficit is created predominantly in the closure region. The shape

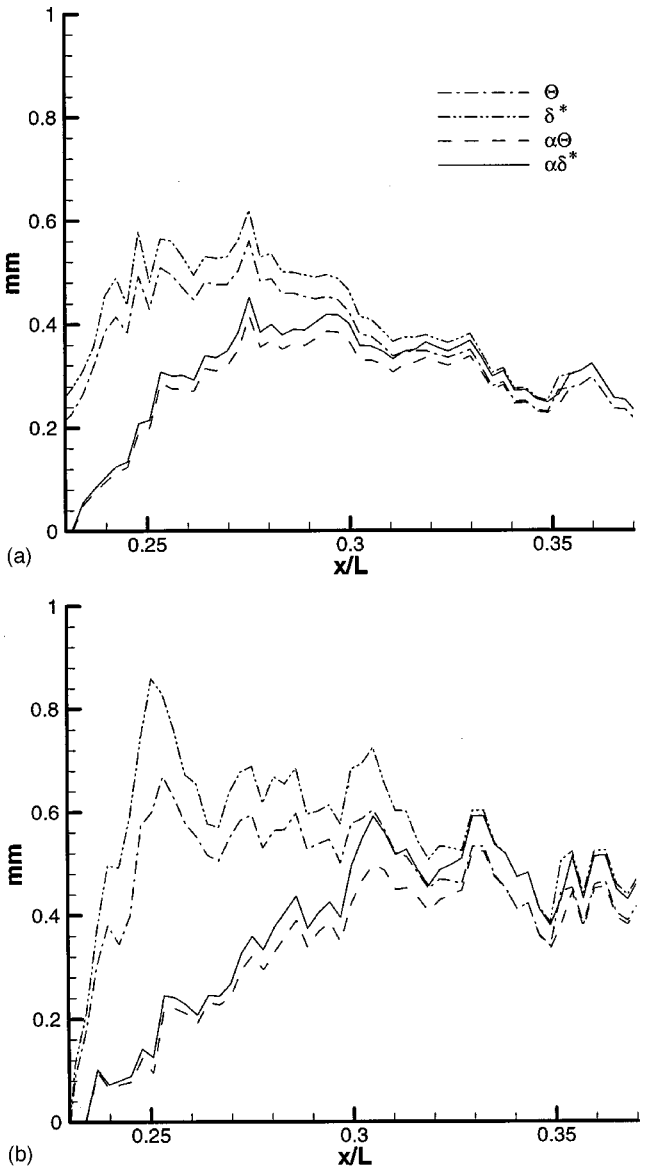

FIG. 22. Momentum and displacement thickness for (a) σ=4.69 and (b) σ=4.41.

factor $\delta^*/\theta \sim 1.2$, which presently occurs at $x/L = 0.25-0.35$, is characteristic to turbulent boundary layers.[56]

VI. SUMMARY AND CONCLUSION

Particle image velocimetry is used to resolve the flow structure in the closure region and downstream of attached cavitation. The present paper focuses on the flow when the ambient pressure is reduced only slightly below the cavitation inception level, i.e., when the cavity is thin (3–5 mm). Two sets of vector maps recorded at the same hydrodynamic conditions but at slightly different water temperatures, 35 °C and 45 °C, provide data on the effect of small changes to the cavitation index (4.69 vs 4.41) on the instantaneous and averaged flow structure, turbulence and vorticity production.

The instantaneous velocity distributions show that when the cavity is thin there is no reverse flow downstream and below the cavitation, i.e., there is no reentrant flow. Instead, the cavities collapse as the vapor condenses. Note that this conclusion applies to conditions where, in the absence of cavitation, there are no adverse pressure gradients in the closure region (there are substantial adverse pressure gradients when cavitation occurs). As discussed in Ref. 32, reverse flow and a reentrant jet start developing when the closure region is located in a region with adverse pressure gradient even without cavitation. Consistent with this conclusion, we do see reverse flow when the cavitation is extended to the diverging part of the present nozzle.

The shape of the cavities in the closure region is highly irregular and unsteady. The flow measurements and high-speed photographs show that the process of cavity collapse involves rollup of large hairpin-like vortices and substantial vorticity production. These vortices extend to elevations that are considerably higher than the height of the stable part of the cavitation. Ensemble averaging of the velocity distributions shows that the unsteady cavity collapse involves substantial increases in turbulence, momentum and displacement thickness in the boundary layer. The small decrease in cavitation index between the two data sets increases the height and length of the cavity, and has a strong impact on the turbulence level and momentum deficit in the boundary layer downstream of the cavitation. The region with the highest turbulence level is located just downstream of the closure region. The Reynolds shear stresses reach levels of 25%–40% of the normal stresses. Such high correlations are characteristic of flows containing large coherent vortex structures, consistent with the observations. However, unlike typical turbulent shear flow, the large eddies (i.e., turbulence production) originate as the vapor cavities collapse.

It is demonstrated that in dealing with the ensemble-averaged flow in the closure region of the attached cavitation, one should account for the sharp gradients in the liquid void fraction. Since the collapse process occurs over a finite region, the incompressible 2D continuity equation can be satisfied only when α_l is included in the analysis. Using the momentum equation it is possible to estimate the magnitude of the ''interaction term,'' i.e., the impact of the vapor phase on the liquid momentum. It is demonstrated from the experimental data that, at least for the present test conditions, the interaction term can be estimated as the local pressure multiplied by the gradient in void fraction. Equation (11) is the resulting ensemble-averaged momentum equation.

ACKNOWLEDGMENTS

This project has been funded by ONR, under Grant No. N00014-95-1-0329. The program manager is Dr. E. Rood. The authors would like to thank Ye Zhang, Mancang Tian, Steven King and Manish Sinha for their valuable contributions.

[1] A. Kubota, H. Kato, H. Yamaguchi, and M. Maeda, ''Unsteady structure measurement of cloud cavitation on a foil section using conditional sampling technique,'' J. Fluids Eng. **111**, 204 (1989).
[2] V. H. Arakeri, A. J. Acosta, ''Viscous effects in the inception of cavitation axisymmetric bodies,'' J. Fluids Eng. **95**, 519 (1973).
[3] E. M. Gates, A. J. Acosta, ''Some effects of several free stream factors on cavitation inception on axisymmetric bodies,'' Proc. 12th Symp. Naval Hydrodynamics, Washington, DC (1978), 86–108.

[4]J. Katz, ''Cavitation phenomena within regions of flow separation,'' J. Fluid Mech. **140**, 497 (1984).
[5]C. Y. Li and S. L. Ceccio, ''Interaction of single traveling bubbles with the boundary layer and attached cavitation,'' J. Fluid Mech. **323**, 329 (1996).
[6]R. E. A. Arndt, J. W. Holl, J. C. Bohn, and W. T. Bechtel, ''The influence of surface irregularities on cavitation performance'' J. Ship Res. **23**, 157 (1979).
[7]E. M. Harvey, W. D. McElroy, and A. H. Whiteley, ''On cavity formation in water,'' J. Appl. Phys. **18**, 162 (1947).
[8]A. J. Acosta and H. Hamaguchi, ''Cavitation inception on the ITTC standard headform,'' Rep. No. E-149.1, Hydrodynamics Laboratory, Caltech (1967).
[9]F. B. Peterson, ''Cavitation originating at liquid-solid interfaces,'' DT-NSRDC Rep. No. 2799 (1968).
[10]M. Tulin, ''Steady two dimensional flows about slender bodies,'' DTMB Tech. Rep. 834 (1953).
[11]M. P. Tulin, ''Supercavitating flow past foils and struts,'' Proc. NPL Symp. Cavitation Hydrodyn. (1955), paper no. 16, pp. 1–19.
[12]M. P. Tulin, ''Supercavitating flows—small perturbation theory,'' J. Ship Res. **7**(3), 16 (1964).
[13]M. Tulin and C. Hsu, ''New applications of cavity flow theory,'' Proc. 13th Symp. Naval Hydrodynamics, Tokyo (1980).
[14]T. Y. Wu, ''A wake model for free-stream flow theory. Part 1: Fully and partially developed wake flows and cavity flows past an oblique flat plate,'' J. Fluid Mech. **13**, 161 (1962).
[15]T. Wu, ''Cavity and wake flows,'' Annu. Rev. Fluid Mech. **4**, 243 (1972).
[16]K. R. Laberteaux and S. L. Ceccio, ''Flow in the closure region of closed partial attached cavitation,'' Third International Symposium on Cavitation, Grenoble, France (1998), pp. 197–202.
[17]R. A. Furness and S. P. Hutton, ''Experimental and theoretical studies of two-dimensional fixed-type cavities,'' J. Fluids Eng. **97**, 515 (1975).
[18]A. Kubota, H. Kato, and H. Yamaguchi, ''A new modeling of cavitating flows: A numerical study of unsteady cavitation on a hydrofoil section,'' J. Fluid Mech. **240**, 59 (1992).
[19]C. Brennen, G. Reisman, and Y. C. Wang, ''Shock waves in cloud cavitation,'' Proc. 21st Symp. Naval Hydrodynamics (1996), pp. 756–771.
[20]Y. Kawanami, H. Kato, H. Yamaguchi, M. Tanimura, and Y. Tagaya, ''Mechanism and control of cloud cavitation,'' J. Fluids Eng. **119**, 788 (1997).
[21]K. A. Morch, ''On the collapse of cavity cluster in flow cavitation'' Proc. 1st Intnl. Conf. on Cavitation and Inhomogeneities in underwater Acoustics, Springer Series in Electrophysics, No. 4 (1980), pp. 95–100.
[22]K. A. Morch, ''Cavity cluster dynamics and cavitation erosion,'' ASME Cavitation and Polyphase Flow Forum (1981), pp. 1-10.
[23]Y. C. Wang and C. E. Brennen, ''Shock wave development in the collapse of a cloud of bubbles,'' ASME Cavitation and Multiphase Flow Forum (1994), pp. 15–19.
[24]L. Noordzij and L. van Wijngaarden, ''Relaxation effects, caused by relative motion, on shock waves in gas-bubble/liquid mixtures,'' J. Fluid Mech. **66**, 115 (1974).
[25]Y. Matsumoto, ''Bubble dynamics in cavitation,'' Third International Symposium on Cavitation, Grenoble, France (1998), pp. 3–8.
[26]F. Avellan, P. Dupont, and I. Ryhming, ''Generation mechanism and dynamics of cavitation vortices downstream of a fixed leading edge cavity,'' Proc. 17th Symp. Naval Hydrodynamics (1988), pp. 317–329.
[27]F. Larrarte, A. Pauchet, Ph. Bousquet, and D. H. Fruman, ''On the morphology of natural and ventilated cavities,'' ASME Cavitation and Multiphase Flow, FED-210 (1995), pp. 31–38.
[28]D. F. de Lange, G. J. de Bruin, and L. van Wijngaarden, ''On the mechanism of cloud cavitation-experiments and modeling,'' 2nd International Symposium on Cavitation (1994), pp. 45–50.
[29]Y. T. Shen and F. B. Peterson, ''Unsteady cavitation on an oscillating hydrofoil,'' Proc. 12th Symp. Naval Hydrodynamics (1978), pp. 362–384.
[30]P. A. Lush and S. R. Skipp, ''High speed cine observation of cavitating flow in a duct,'' Int. J. Heat Fluid Flow **7**, 283 (1986).
[31]Q. Le, J. P. Franc, and J. M. Michel, ''Partial cavities: Global behavior and mean pressure distribution,'' J. Fluids Eng. **115**, 243 (1993).
[32]M. Callenaere, J. P. Franc, and J. M. Michel, ''Influence of cavity thickness and pressure gradients on the unsteady behavior of partial cavities,'' Third International Symposium on Cavitation, Grenoble, France (1998), pp. 209–214.
[33]R. Dong, S. Chu, and J. Katz, ''Quantitative visualization of the flow structure within the volute of a centrifugal pump, Part A: Technique,'' J. Fluids Eng. **114**, 390 (1992).
[34]R. Dong, S. Chu, and J. Katz, ''Quantitative visualization of the flow structure within the volute of a centrifugal pump, Part B: Results,'' J. Fluids Eng. **114**, 396 (1992).
[35]S. Chu, S. Dong, and J. Katz, ''Relationship between unsteady flow, pressure fluctuations and noise in a centrifugal pump. Parts A: Use of PDV data to compute the pressure field,'' J. Fluids Eng. **117**, 24 (1995).
[36]S. Chu, S. Dong, and J. Katz, ''Relationship between unsteady flow, pressure fluctuations and noise in a centrifugal pump. Part B: Effects of blade-tongue interactions,'' J. Fluids Eng. **117**, 30 (1995).
[37]R. R. Dong, J. Katz, and T. T. Huang, ''On the structure of bow waves on a ship model,'' J. Fluid Mech. **346**, 77 (1997).
[38]R. Dong, S. Chu, and J. Katz, ''Effect of modification to tongue and impeller geometry on unsteady flow, pressure fluctuations and noise in a centrifugal pump,'' J. Turbomachinery **119**, 506 (1997).
[39]G. Sridhar and J. Katz, ''Lift and drag forces on microscopic bubbles entrained by a vortex,'' Phys. Fluids **7**, 389 (1995).
[40]G. Sridhar and J. Katz, ''Effect of entrained bubbles on the structure of vortex rings,'' J. Fluid Mech. **397**, 171–202 (1999).
[41]S. Liu, C. Meneveau, and J. Katz, ''On the properties of similarity subgrid-scale models as deduced from measurements in a turbulent jet,'' J. Fluid Mech. **275**, 83 (1994).
[42]M. Sinha and J. Katz, ''Flow structure and turbulence in a centrifugal pump with a vaned diffuser,'' Proc. ASME Fluids Engineering Division, Washington, DC (1998).
[43]G. Roth, D. Hart, and J. Katz, ''Feasibility of using the L64720 video motion estimation processor (MEP) to increase efficiency of velocity map generation for PIV,'' ASME/EALA Sixth International Symposium on Laser Anemometry, Hilton Head, SC (1995).
[44]L. M. Lourenco and K. Krothapalli, ''On the accuracy of velocity and vorticity measurements with PIV,'' Exp. Fluids **18**, 421 (1995).
[45]R. D. Keane and R. J. Adrian, ''Optimization of particle image velocimeters. Part I: Double pulsed systems,'' Meas. Sci. Technol. **1**(11), 963 (1990).
[46]V. H. Arakeri, ''Viscous effects on the position of cavitation separation from smooth bodies,'' J. Fluid Mech. **68**, 779 (1975).
[47]J. P. Franc and J. M. Michel, ''Attached cavitation and the boundary layer: experimental investigation and numerical treatment,'' J. Fluid Mech. **154**, 63 (1985).
[48]A. L. Tassin and S. L. Ceccio, ''Examination of the flow near the leading edge of attached cavitation. Part 1. Detachment of two-dimensional and axisymmetric cavities,'' J. Fluid Mech. **376**, 61 (1998).
[49]B. Gindroz and M. L. Billet, ''Nuclei and propeller cavitation inception,'' ASME Symposium on Cavitation and Gas-Liquid Flow in Fluid Machinery and Devices (1994), FED-190, pp. 251–260.
[50]C. Brennen, ''Cavity surface waves pattern and general appearance,'' J. Fluid Mech. **44**, 33 (1970).
[51]Y. Zhang, S. Gopalan, and J. Katz, ''On the flow structure and vorticity production due to sheet cavitation,'' Proc. ASME Fluids Engineering Summer Meeting, FEDSM98-5301, Washington, DC (1998).
[52]J. Zhang, B. Tao, and J. Katz, ''Turbulent flow measurement in a square duct with hybrid holographic PIV,'' Exp. Fluids **23**, 373 (1997).
[53]D. A. Drew and R. T. Lahey, Jr., ''Analytical modeling of multiphase flow,'' in *Particulate two-phase flow,* edited by M. C. Roco (Butterworth-Heinemann, Washington, DC, 1993), pp. 509–566.
[54]J. O. Hinze, *Turbulence—2nd Edition* (McGraw-Hill, New York, 1975).
[55]J. K. Eaton and J. P. Johnson, ''Turbulent flow reattachment: An experimental study of the flow and structure behind A backward-facing step,'' Report MD-39, Department of Mechanical Engineering, Stanford University (1980).
[56]L. C. Burmeister, *Convective Heat Transfer* (Wiley, New York, 1993).